1	Anisotropic and Viscoelastic Tensile Mechanical Properties of
2	Aponeurosis: Experimentation, Modeling, and Tissue
3	Microstructure
4	
5	
6	Keith L. Grega
7	Biomedical Engineering
8	Bucknell University, Lewisburg PA
9	
10	Ruth N. Segall
11	Cell Biology/Biochemistry
12	Bucknell University, Lewisburg PA
13	
14	Anurag J. Vaidya
15	Biomedical Engineering
16	Bucknell University, Lewisburg PA
17	
18	Chong Fu
19	Mechanical Engineering
20	Bucknell University, Lewisburg PA
21	
22	Benjamin B. Wheatley*
23	Mechanical Engineering
24	Bucknell University
25	1 Dent Drive
26	Lewisburg, PA 17837
27	b.wheatley@bucknell.edu
28	570-577-3883
29	
30	Keywords: biaxial testing, modulus, constitutive modeling, finite element analysis, scanning electron
31	microscopy
32	* Corresponding outhor
33	* Corresponding author

Abstract

35

36

37

38

39

40

41 42

43

44

45

46

47 48

49

50

51

52

Aponeuroses are stiff sheath-like components of the muscle-tendon unit that play a vital role in force transmission and thus locomotion. There is clear importance of the aponeurosis in musculoskeletal function, but there have been relatively few studies of aponeurosis material properties to date. The goals of this work were to: 1) perform tensile stress-relaxation tests, 2) perform planar biaxial tests, 3) employ computational modeling to the data from 1 and 2, and 4) perform scanning electron microscopy to determine collagen fibril organization for aponeurosis tissue. Viscoelastic modeling and statistical analysis of stress-relaxation data showed that while relaxation rate differed statistically between strain levels (p=0.044), functionally the relaxation behavior was nearly the same. Biaxial testing and associated modeling highlighted the nonlinear (toe region of ~2-3% strain) and anisotropic (longitudinal direction linear modulus ~50 MPa, transverse ~2.5 MPa) tensile mechanical behavior of aponeurosis tissue. Comparisons of various constitutive formulations showed that a transversely isotropic Ogden approach balanced strong fitting (goodness of fit 0.984) with a limited number of parameters (five), while damage modeling parameters were also provided. Scanning electron microscopy showed a composite structure of highly aligned, partially wavy collagen fibrils with more random collagen cables for aponeurosis microstructure. Future work to expand microstructural analysis and use these data to inform computational modeling would benefit this work and the field.

1. Introduction

Aponeuroses are stiff sheath-like components of the muscle-tendon unit that play a vital role in force transmission and thus locomotion (Eng and Roberts, 2018; Bojsen-Møller and Magnusson, 2019). While aponeurosis has traditionally been viewed as an extension of the tendon that mechanically acts in series with muscle, this has been shown to not be the case, and has led to improper assumptions regarding the function of aponeurosis (Herzog, 2019). Various experimental and computational studies have shown a complex relationship between aponeurosis deformation and muscle force, both active and passive (Arellano et al., 2016). Specifically, incisions of the aponeurosis in lateral gastrocnemius muscles of wild turkeys altered the gearing and force relationship in the muscle (Eng and Roberts, 2018). Varying the width, length and thickness of the aponeurosis in a 3D muscle model has also shown to have a significant impact on peak stretch location and magnitude of muscle (Rehorn and Blemker, 2010). However, the specific contributions that each fibrous tissue has on muscle-tendon unit mechanics is still not fully understood (Herzog, 2017).

There is clear importance of the aponeurosis in musculoskeletal function, but there have been relatively few studies of aponeurosis material properties to date (Azizi et al., 2009; Bojsen-Møller and Magnusson, 2019; Shan et al., 2019). Determining the material properties of the aponeurosis will provide evidence of its structure and function to identify how it contributes to the movement of the musculoskeletal system. Azizi et al measured uniaxial tensile material propertie in turkey gastrocnemius aponeurosis, exhibiting the highly anisotropic nature of the tissue due to the aligned collagen structure in the longitudinal or along-fiber direction (Azizi et al., 2009). While some studies have explored structural mechanical properties such as stiffness (Kitaoka et al., 1994; Scott and Loeb, 1995), this leaves a distinct lack of data on the material properties of aponeurosis such as modulus, especially in comparison to other orthopaedic tissues. While there is some debate regarding the similarities and differences of the aponeurosis and tendon, one of the main physiological differences between the tendon and aponeurosis is that the tendon is free from muscle fascicles with the exception of the myotendinous junction, while the aponeurosis spreads over a large portion of the muscle belly. It has been shown that during muscle force production, transverse stretch in the aponeurosis exceeds stretch in the longitudinal direction by roughly a factor of four (Azizi and Roberts, 2009). Therefore, it can be inferred that the aponeurosis is subject to biaxial load during muscle contraction, unlike tendon which is primarily subject to uniaxial load. However, studies of aponeurosis material properties have been completed under uniaxial stretch only (Azizi et al., 2009; Shan et al., 2019), despite a clear need to investigate biaxial aponeurosis stretch.

Additionally, many soft tissues exhibit time dependent (viscoelastic) behavior such as stress relaxation (Johnson et al., 1994; Provenzano et al., 2001), and while aponeurosis is also viscoelastic (Pavan et al., 2011), literature data are limited. Aponeurosis stores and returns energy during locomotion (Wager and Challis, 2016), which is affected by tissue viscoelasticity. To the authors' knowledge there has been one study on stress relaxation of plantar aponeurosis (Pavan et al., 2011), which has a distinctly different role and deformation state than typical aponeurosis that acts as a sheath over muscle. While skeletal muscle has shown some degree of nonlinear viscoelasticity – a dependence of stress relaxation behavior on the level of tensile strain (Wheatley et al., 2016a, 2016c), tendon is generally observed to be quasi-linear

viscoelastic – where stress relaxation is independent of strain level (Pioletti and Rakotomanana, 2000). It remains unknown if sheath aponeurosis exhibits nonlinear or quasi-linear viscoelastic behavior. Thus, there exists a need to better understand the time dependent material properties of aponeurosis tissue.

While determining material properties of aponeurosis can provide quantitative insight into muscle-tendon unit function, they are most useful in developing and employing computational models of the musculoskeletal system. Approaches to model muscle-tendon units range from classical Hill-type models (Ackland et al., 2012), more geometrically complex finite element simulations (Tsui et al., 2004; Wheatley et al., 2018), and larger scale simulations of whole human movement (Rajagopal et al., 2016). These simulations can aid in understanding how a healthy musculoskeletal system functions (Rajagopal et al., 2016) and how disease and impairment can compromise this function (Ong et al., 2019). To properly employ these modeling techniques, however, we must have a comprehensive understanding of how aponeurosis behaves as a mechanical component. Thus, there exists a strong need to further explore the tissue-level material properties of aponeurosis, specifically in response to biaxial stretch and under stress-relaxation conditions.

In addition to characterizing and modeling material properties of orthopaedic tissues, microstructural analysis and imaging provides vital insight into tissue morphology. Scanning electron microscopy is a viable method to investigating microstructure in orthopaedic tissues such as tendon (Provenzano and Vanderby, 2006; Herod et al., 2016) and muscle (Mohammadkhah et al., 2017; Sleboda et al., 2020). However, there is a distinct lack of microstructural analysis through use of scanning electron microscopy for aponeurosis tissue, particularly in relation to structure-function relationships. While aponeurosis macrostructure shows highly aligned collagen bundles (Azizi et al., 2009), we hypothesize this is also observed at the microstructural level of collagen fibrils.

Based on the above, we have identified four aims of this research, with the overarching goal of developing a better understanding of aponeurosis mechanical properties:

- developing a better understanding of aponeurosis mechanical properties:
 1) Measure the stress-relaxation behavior of aponeurosis tissue, and determine if it is dependent on strain level (nonlinear viscoelastic or quasi-linear viscoelastic)
 - 2) Perform planar biaxial tensile testing to evaluate aponeurosis tissue stress-stretch response to multi-axial load
 - 3) Employ computational modeling based on the above to develop the appropriate material properties of aponeurosis
 - 4) Perform scanning electron microscopy to determine collagen fibril organization and alignment in aponeurosis

We hypothesize that this approach of materials testing, imaging, and modeling will further elucidate the mechanics of aponeurosis tissue. Future use of these data in computational models of muscle-tendon units can aid in understanding locomotion and neuromuscular impairments.

2.1 Sample Preparation

For all testing, porcine shoulder samples were obtained from a local abattoir and the triceps brachii aponeurosis (Figure 1A) was dissected from the muscle using standard dissection tools. Long and steady cuts using sharp dissection blades were used to ensure minimal damage to the aponeurosis. As much muscle tissue as possible was removed without tearing or damaging the aponeurosis (Azizi et al., 2009; Shan et al., 2019). All samples were kept moist by applying PBS throughout the dissection process and before testing (Azizi and Roberts, 2009; Azizi et al., 2009). Each sample was speckled with graphite powder to enhance digital image correlation strain tracking during testing (Lynch et al., 2003; Luyckx et al., 2014). Graphite washout was prevented by gently dabbing the sample surface with dry gauze before applying the speckle. Postmortem effects were assumed negligible due to similar assumptions made for tendon (Evans and Barbenel, 1975). Each sample's thickness was measured using a dissection microscope by taking images across the entire length of the aponeurosis and averaging all of the measurements (Figure 1B). We differentiated the aponeurosis tissue from the muscle tissue under the microscope by its distinctive silver coloration compared to muscles red coloration. To acquire thickness measurements across the entire length of the sample, nine images were obtained, and four measurements were taken off each image with image acquisition software (ThorCam, Thorlabs, Inc.).

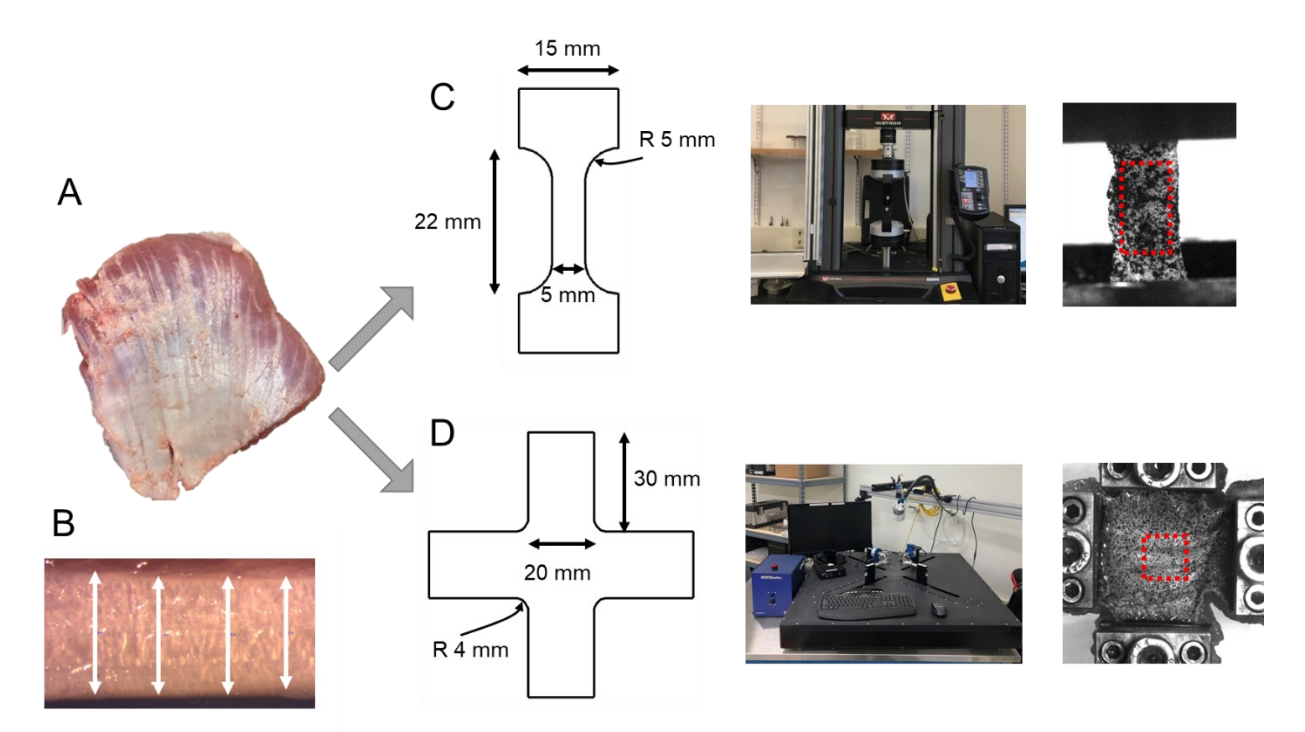


Figure 1. Overview of experimental workflow. A) Triceps brachii muscle with attached aponeurosis (sliver sheath). B) Light microscope image for thickness measurements (white arrows). C) Dog bone sample, uniaxial material testing instrument, and example digital image correlation image with highlighted region of interest (red rectangle). D) Cruciform sample, planar biaxial material testing instrument, and example digital image correlation image with with highlighted region of interest (red square).

2.1 Stress Relaxation Testing

Four porcine shoulders were obtained from a local abattoir to extract the triceps brachii muscle for testing. The aponeurosis samples were cut into dog bone samples approximately 22 mm in height by 5 mm in width (Figure 1C) (Azizi et al., 2009). All samples were cut parallel to the muscle fiber direction (n=20). Tensile stress relaxation was performed on each sample with a 5965 Instron uniaxial testing system with a 5 kN load cell (Figure 1C). Two dimensional images were acquired approximately every 0.25 seconds throughout each test to determine the precise strain of each sample using a digital image and correlation software (Azizi et al., 2009; Wheatley et al., 2016b). The employed test procedure was as follows: 20 cycles of preconditioning (between 0.5 N and 1 N), then two consecutive stress relaxation steps of approximately 1-2% sample engineering strain at a rate of 1-2%/sec and 300 seconds of relaxation (Komatsu et al., 2007). Engineering stress (Equation 1) was calculated from force F and initial specimen area A_0 . Engineering strain for each stress relaxation ramp was determined with digital image correlation over a rectangular region of interest comprising the width of the sample and approximately 5 mm in height above and below the centerline (Figure 1C). Stress data were then fit to a power law (Equation 2), which characterized the rate of relaxation with a b parameter.

174 175 176

177

180

181

182 183

184

185 186

187

188

189

190

191

192

193

194

195

196 197

198

160

161

162

163

164 165

166 167

168

169

170

171

172

173

$$\sigma = \frac{F}{A_0} \tag{1}$$

$$\sigma = at^b + C \tag{2}$$

$$\sigma = at^b + C \tag{2}$$

178 179 2.2 Biaxial Tensile Testing

> Similar to fascia samples (Eng et al., 2014), aponeurosis samples were cut into cruciform shapes approximately 30 mm in arm length and 20 mm in arm width by a custom die (Figure 1D). All samples (n=9) were punched such that the aponeurosis fibers were best aligned with one orientation of the cruciform, which was possible due to the highly aligned nature of the tissue and size of the porcine muscle. Samples were speckled with graphite powder similar to stress-relaxation testing (Figure 1D). Biaxial tensile testing was completed in a planar biaxial material testing system (ADMET, Inc.) with 220 N load cells (Figure 1D). An initial gauge length of approximately 30 mm for each orientation was selected, and the longitudinal direction of the tissue was preloaded to 0.5 N while the transverse direction of the tissue was preloaded to 0.15 N to remove slack. Equibiaxial constant rate tensile testing was then performed at a grip-to-grip strain rate of 0.05%/sec until failure. During testing, images were taken approximately every second and digital image correlation was performed on a 10 mm x 10 mm region of interest centered on the initial image of each sample (Figure 1D). For two-dimensional digital image correlation, longitudinal and transverse stretch were determined for constitutive modeling (Szczesny et al., 2012) (Correlated Solutions, Inc.). Thickness measurements were measured post-hoc from tested samples due to the inability to obtain accurate thickness measurements of the aponeurosis in the region of interest without damaging the tissue. The cruciform samples were cut at 45-degree angles between each arm making an "X" in the middle of the sample. Five measurements were taken from each cut and all of the measurements were averaged together to obtain the overall thickness in the region of interest. Regions with clear damage were avoided for thickness measurements. This method was chosen due to the failure

mechanism of aponeurosis tissue (rupture versus plastic deformation) and the similarities in measured thickness between stress-relaxation and biaxial samples.

Nominal stress in both the longitudinal and transverse direction was determined for each sample using the force values from MTESTQuattro and the thickness and arm length measurements. The nominal stress value in the arm of each sample was multiplied by a cofactor to determine the stress in the center of the cruciform sample similar to (Labus and Puttlitz, 2016). The cofactor was determined via a finite element modeling protocol similar to previous modeling approaches of biaxially stretched, soft, fibrous tissues (Jacobs et al., 2013). A quarter-symmetric cruciform finite element model with a 25 mm² square region of interest was developed in FEBio (Figure 2A) (Maas et al., 2012). The average Cauchy stress data in the x or y direction from the region of interest was compared to the nominal stress in the corresponding cruciform arm. By employing a transversely isotropic neo-Hookean material model, a graph of correction factor versus stretch was created to determine the trend between the correction factor values and the various strain levels in both the x and y direction (Figure 2B) (Jacobs et al., 2013). To determine the appropriate correction factor functions for the longitudinal and transverse directions, piecewise functions were fit to model correction factor data points (Figure 2B).

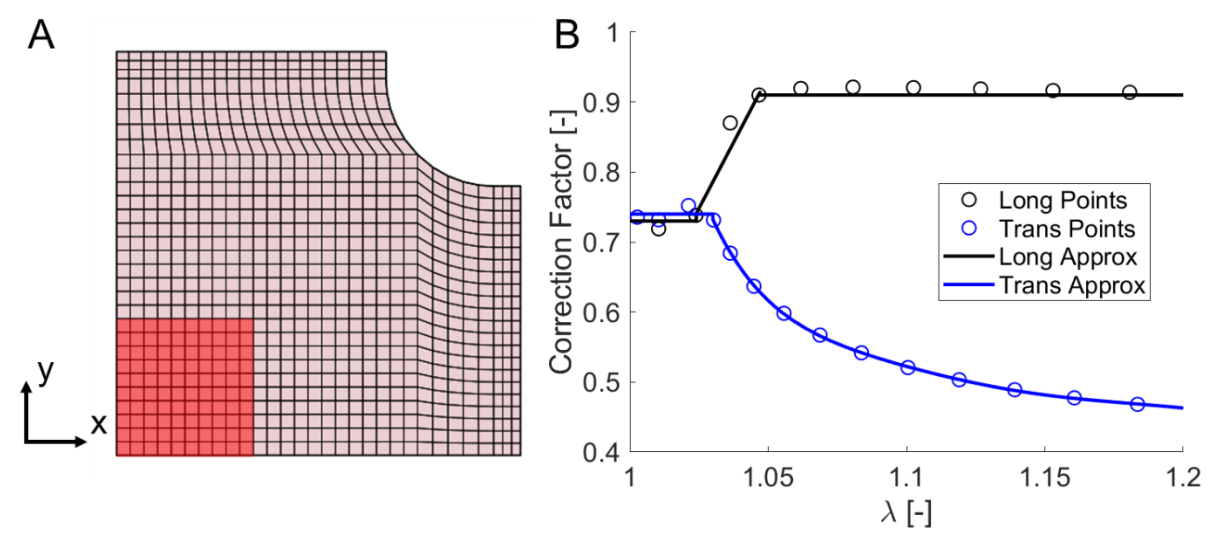


Figure 2. A) Quarter symmetric finite element model for correction factor modeling. B) Correction factor model outputs (circles) and approximated correction factor piecewise functions (solid curves).

2.3 Modeling

2.3.1 Viscoelastic Modeling

To characterize relaxation behavior of the aponeurosis, a three term Prony series quasi-linear viscoelastic model (Equations 3-4) was fit to both a normalized hold phase stress from both the stretches and an average hold phase stress from both the stretches (Chen, 2000).

227
$$\sigma(\varepsilon,t) = \int_0^t E(t-\xi) \, \frac{d\varepsilon(\xi)}{d\xi} d\xi \tag{3}$$

228
$$E(t) = E_0 \left(1 - \sum_{i=1}^{3} E_i \left[1 - \exp\left(-\frac{t}{\tau_i}\right)\right]\right)$$
 (4)

Here stress σ is calculated from the convolution integral (Equation 3), which includes the Prony series reduced relaxation function E(t), nominal strain ε , and an integration parameter ξ . This includes three relaxation coefficients E_i , three time constants τ_i , and the instantaneous modulus E_0 . As the purpose of this analysis was to compare relaxation behavior only, $E_0=1$ was fixed and all data were normalized. Parameter determination was performed in two steps: a Monte Carlo simulation followed by a nonlinear least-squares deterministic optimization (lsqnonlin in MATLAB) (Vaidya and Wheatley, 2019). In the Monte Carlo simulation, the six parameters (E_{1-3} and τ_{1-3}) were randomly varied for 100,000 simulations, ensuring $0 < E_1 + E_2 + E_3 < 1$. The set of parameters minimizing percent error between the normalized model and experimental hold stress was used as initial guesses for the deterministic optimization, which optimized percent difference between normalized model and experimental hold stresses.

2.3.1 Hyperelastic Modeling

Adjusted biaxial stress-stretch data were fit to a range of hyperelastic constitutive models through inverse finite element analysis in FEBio (Maas et al., 2012; Wheatley et al., 2015). A finite element representation of the 10 mm x 10 mm region of interest was developed using quarter symmetry. This simple geometric model was subject to longitudinal and transverse stretch boundary conditions from the mean digital image correlation data. Longitudinal and transverse model stress were output by averaging the Cauchy stress for each element in each orientation. The model stress-stretch outputs were then fit to experimental mean stress-stretch data by varying model parameters (specific parameters outlined below) within *lsqnonlin* in MATLAB similar to the viscoelastic modeling approach. A total of five constitutive models were identified and implemented that ranged in nonlinearity, fiber definition, and material damage. For hyperelastic modeling, the constitutive relation is defined by the strain energy density function Ψ (Equation 5, where σ is the Cauchy stress, J is the volume ratio of the solid, F is the deformation gradient, and $C = F^T F$ is the right Cauchy-Green deformation tensor). The strain energy density function for anisotropic materials such as aponeurosis can be decomposed into isotropic and anisotropic components (Equation 6). The isotropic component is typically referred to as an isotropic ground matrix while the anisotropic component generally represents collagen fibers in soft tissues.

$$\sigma = 2J^{-1}F\frac{\partial \Psi}{\partial c}F^{T} \tag{5}$$

$$\Psi_{\text{tot}}(\mathbf{C}) = \Psi_{\text{iso}}(\mathbf{C}) + \Psi_{\text{aniso}}(\mathbf{C})$$
 (6)

For this work, we have identified two isotropic strain energy density terms commonly used for biological and engineered materials subject to large strains, the Mooney-Rivlin formulation (Ψ^{MR}) and a first-order Ogden formulation (Ψ^{OG}). The Mooney-Rivlin (MR) model is a function of the first and second invariants I_1 and I_2 of C and includes two shear modulus-like parameters c_1 and c_2 (Equation 7). The

Ogden model is a summation function of the principal stretches λ_i of the deformation and requires specification of moduli-like parameters c_i and nonlinear parameters m_i (Equation 8). For simplicity and reduction of parameters, in this work we have chosen a first-order Ogden model (N = 1).

269

266

267

268

270

271

$$\Psi^{MR}(I_1, I_2) = c_1(I_1 - 3) + c_2(I_2 - 3) \tag{7}$$

$$\Psi^{MR}(I_1, I_2) = c_1(I_1 - 3) + c_2(I_2 - 3)$$

$$\Psi^{Ogden}(\lambda_1, \lambda_2, \lambda_3) = \sum_{i=1}^{N} \frac{c_i}{m_i} \left(\lambda_1^{m_i} + \lambda_2^{m_i} + \lambda_3^{m_i} - 3 \right)$$
(8)

272 273

274

275

276

277

The specific formulations presented in Equations 7-8 are generic forms of these models, and for finite element implementation they must be adapted to include the material response to volumetric deformations. These complete, isotropic coupled equations are provided for the Mooney-Rivlin model $(\Psi_{iso}^{MR}$ Equation 9) and Ogden model $(\Psi_{iso}^{Ogden}$ Equation 10) and each include a bulk-like modulus parameter k. This parameter dictates the response to volumetric deformations, as characterized by the volume ratio *I*.

278 279

$$\Psi_{\text{iso}}^{\text{MR}}(I_1, I_2, J) = c_1(I_1 - 3) + c_2(I_2 - 3) - 2(c_1 + 2c_2)\ln J + \frac{k}{2}(\ln J)^2$$
(9)

281
$$\Psi_{\text{iso}}^{\text{Ogden}}(\lambda_1, \lambda_2, \lambda_3, J) = \sum_{i=1}^{N} \frac{c_i}{m_i} \left(\lambda_1^{m_i} + \lambda_2^{m_i} + \lambda_3^{m_i} - 3 - m_i \ln J \right) + \frac{k}{2} (\ln J)^2$$
 (10)

282 283

284

285 286

287

288

For material anisotropy, nonlinear tension-only fibers were embedded into the isotropic ground matrix. The constitutive relation for these fibers (Ψ^f_{aniso} , Equation 11) is a piecewise function that enacts this tension-only response and is a function of the fiber stretch λ_f . The material parameters for this relation include a transition stretch λ_f^* where the fiber transitions from a nonlinear power law response to a linear response, a power law parameter β and a fiber modulus E. It should be noted that parameters A, B, and C are calculated to enforce continuity of strain energy density. This fiber material model can be included in the overall material response in FEBio using the solid mixture material (Maas et al., 2012).

289 290

$$\Psi_{\text{aniso}}^{f}(\lambda_{f}^{2}) = \begin{cases} 0, & \lambda_{f} \leq 1 \\ \frac{A}{2\beta} (\lambda_{f}^{2} - 1)^{\beta}, & 1 < \lambda_{f} < \lambda_{f}^{*} \\ E(\lambda_{f}^{*} - \lambda_{f}) + B(\lambda_{f}^{2} - \lambda_{f}^{*2}) + C, & \lambda_{f}^{*} \geq \lambda_{f} \end{cases}$$

$$(11)$$

292 293

294

295

296

297

298

299

300

The final constitutive formulation that was explored in this work was reactive damage modeling (Safa et al., 2018). In continuum damage modeling applications, the strain energy density function is reduced linearly with accumulated material damage D (Equation 12). For this work, material damage was specified with respect to two conditions – the initiation of damage and the accumulation of damage. Here initiation was chosen as the normal Lagrange strain for the reinforcing fibers and assuming that damage can only accumulate (this work does not consider the effects of healing and regeneration), we defined the damage accumulation with a log-normal cumulative distribution function (Equation 13, where Ξ is the damage criterion, in this case normal Lagrange strain, µ dictates the value of \(\mathbb{E} \) where 50% damage has

occurred, and σ dictates the rate of damage accumulation). We also assumed that the maximum amount of damage was 100%, or $D_{max} = 1$.

$$\Psi_{\mathbf{r}}(\mathbf{C}, D) = (1 - D)\Psi \tag{12}$$

$$D(\Xi) = \frac{1}{2} \operatorname{erfc} \left[-\frac{\ln\left(\frac{\Xi}{\mu}\right)}{\frac{\sigma}{2}} \right]$$
 (13)

A total of five different constitutive models were fit to experimental data. These included 1) transversely isotropic Mooney-Rivlin, 2) transversely isotropic Ogden, 3) Mooney-Rivlin with two fiber families, 4) transversely isotropic Ogden with longitudinal fiber damage, and 5) Mooney-Rivlin two fiber families with longitudinal damage. For all models the bulk-like modulus was fixed at k=100 MPa. For Mooney-Rivlin models, a $c_1=c_2$ constraint was applied to ensure unique solutions for optimization fitting.

2.4 Statistical Analysis

The experimental stress relaxation data were analyzed by comparing the power law coefficient b that resulted from the first and second relaxations through a paired two sample t-test for means (significance set at p<0.05) to determine whether the relaxation after the first and second strains of each sample were statistically significant.

The goodness of fit (GoF) for all fits were evaluated with the *goodnessOfFit* function in MATLAB (Equation 15). Here P_i^{mod} and P_i^{exp} are the model and experimental stress values, respectively, at the ith data point and N is the total number of data points. Fits range from $-\infty$ (worst) to 1 (perfect). The overall percent error, peak stress percent error, and normalized root mean square error (NRMSE) were also determined (Equation 16).

$$GoF = 1 - \sum_{i=1}^{N} \left[\frac{P_i^{mod} - P_i^{exp}}{P_i^{mod} - mean(P_i^{exp})} \right]^2$$
 (15)

326
$$RMSE = \sqrt{\frac{\sum_{i=1}^{N} (P_i^{mod} - P_i^{exp})^2}{N}}$$
 (16)

2.5 Scanning Electron Microscopy

Two porcine samples were obtained from a local abattoir to extract the triceps brachii aponeurosis for scanning electron microscopy (SEM). The triceps brachii aponeurosis was dissected by the same procedure as the stress relaxation and biaxial tests, and subject to a fixing a preparation protocol for imaging (Carson and Cappellano, 1997). The samples were cut into approximately 4 mm x 8 mm rectangles then fixed in 10% formaldehyde for 24 hours at 4 degrees Celsius with a 1:20 volume to fixative ratio. Samples were then subject to a washing alcohol series that included 15 minutes in 70% ethanol, 15 minutes in 90% ethanol, and then a series of 15, 30, then 45 minutes in 100% ethanol. To prepare for dehydration, samples were transferred to a 1:2 solution of HMDS to ethanol for 20 minutes followed by 20 minutes in a 2:1 HMDS to ethanol solution, and finally two cycles of 20 minutes in 100%

HMDS solution. Approximately half of the HMDS in each vial was then discarded and the vials were placed without caps in a vacuum for desiccation. Samples that were dehydrated could then be properly sputter coated with gold approximately 48 to 72 hours later. Scanning electron microscopy was conducted on a Hitachi SU5000 Field Emission Gun microscope. Relevant images were analyzed with the *Directionality* plugin found in Fiji (Schindelin et al., 2012) to determine collagen fibril alignment. The number of bins was set to nineteen and the histogram range was set to 0-180°.

3.1 Stress Relaxation

3. Results

The average thickness of the 20 aponeurosis samples were $0.506~\text{mm} \pm 0.034$ (standard error). The average power law constant of the 20 samples during the first relaxation phase was -0.1013 ± 0.0057 (standard error) and during the second relaxation phase the average power law constant was -0.0893 ± 0.0018 (standard error). The paired t-test comparing the first and second relaxation phases were statistically significant (p=0.044). However, further evaluation of b parameter versus strain percentage data shows minimal variation between the first relaxation (Ramp 1) and the second relaxation (Ramp 2) (Figure 3), as an R^2 value of 0.0291 with a linear slope of 0.0026 was fit to these data. Thus, any strain dependent relaxation may be statistically significant, but minimal.

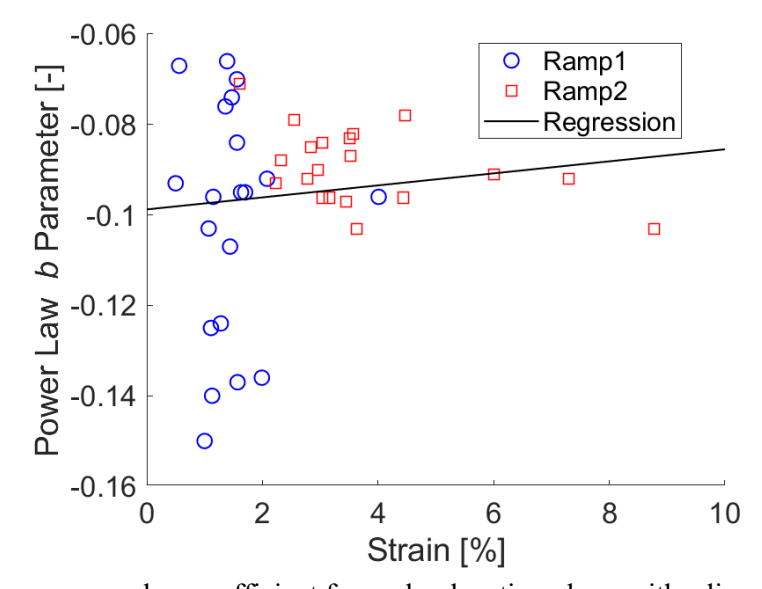


Figure 3. Strain versus power law coefficient for each relaxation phase with a linear regression fit.

Comparison between the experimental viscoelastic behavior data and the viscoelastic model shows similar comparable behaviors (Figure 4). The global stochastic Monte Carlo simulation in conjunction with the deterministic optimization yielded excellent fits between the three-term linear Prony series viscoelastic model and normalized experimental stress data (average percent error = $0.29 \pm 0.01\%$, average RMSE = 0.40 ± 0.02 , average GoF = 1.00) (Figure 4). For the viscoelastic model, the parameters show a similar amount of stress relaxation behavior (G) and similar rate of relaxation (τ) between the first, second, and average relaxations (Table 1), suggesting that the use of a linear or quasi-linear

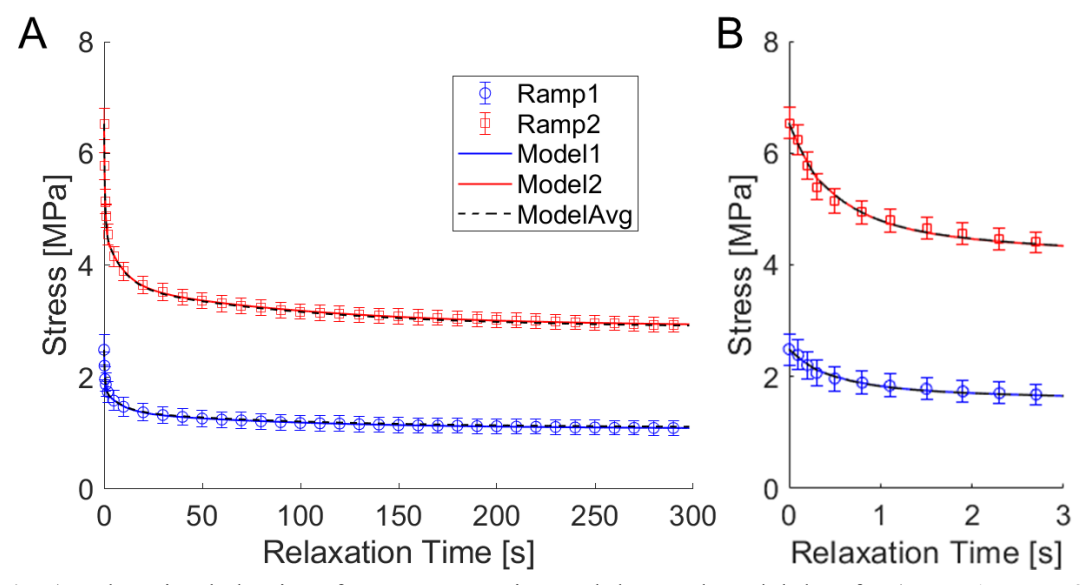


Figure 4. A) Relaxation behavior of average experimental data and model data for (Ramp1, Ramp2, and ModelAvg) over the entire 300 second relaxation periods. B) Highlighted relaxation behavior over the first three seconds of relaxation.

Table 1. Optimized viscoelastic parameters for the hold phase of stress relaxation after first, second, and average of first and second stretches.

Parameter	Ramp One	Ramp Two	Average
G ₁ [MPa]	0.420	0.426	0.423
G ₂ [MPa]	0.135	0.127	0.130
G ₃ [MPa]	0.101	0.0946	0.0978
τ ₁ [s]	0.542	0.541	0.551
τ ₂ [s]	8.59	8.83	8.86
τ ₃ [s]	98.0	101	100

3.2 Biaxial Stretch

Tensile planar equibiaxial stress-stretch data shows consistent anisotropy of aponeurosis tissue (Figure 5). The average thickness of the nine aponeurosis samples were $0.626 \text{ mm} \pm 0.028$ (standard error). Qualitatively, the aponeurosis is shown to be stiffer in the longitudinal direction compared to the transverse direction and strain more in the transverse direction compared to longitudinal (Figure 5A). Quantitatively, these results are supported by the finding that over the course of the experiment the stress ratio leveled out at approximately ten and the strain ratio leveled out at approximately 0.5 between longitudinal and transverse orientations (Figure 5B).

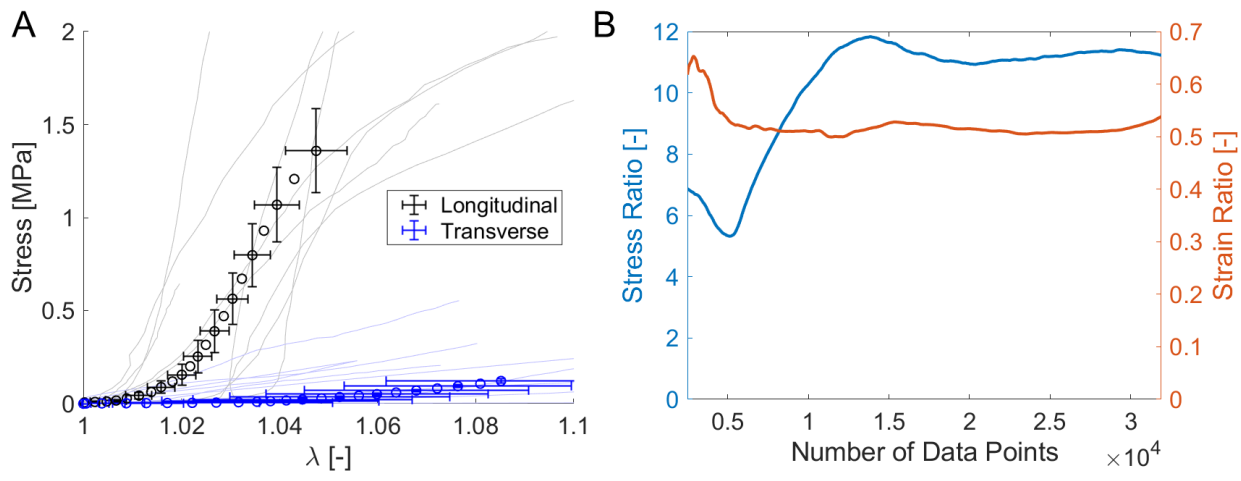


Figure 5. A) Planar equibiaxial tensile stress-stretch data. Raw data are provided in light background curves for longitudinal (black) and transverse (blue) direction. Mean and standard error are shown with open circles and error bars. B) Mean data ratios for stress (blue) and strain (orange) between the longitudinal and transverse directions as a function of data points. Data presented are longitudinal:transverse ratios.

Finite element model fits to experimental data were generally strong as observed both visually (Figure 6) and statistically (Table 2). The model with the worst fit was the transversely isotropic Mooney-Rivlin formulation due to the linear stress-stretch response in the transverse direction (Figure 6B). The best fit was the two fiber families model with longitudinal fiber damage, which produced a root mean square error of 0.00655 MPa. However, this model was statistically nearly identical to the transversely isotropic Ogden damage model, and the non-damage versions of these models had strong fit statistics as well (above a 0.95 goodness of fit value (Table 2)).

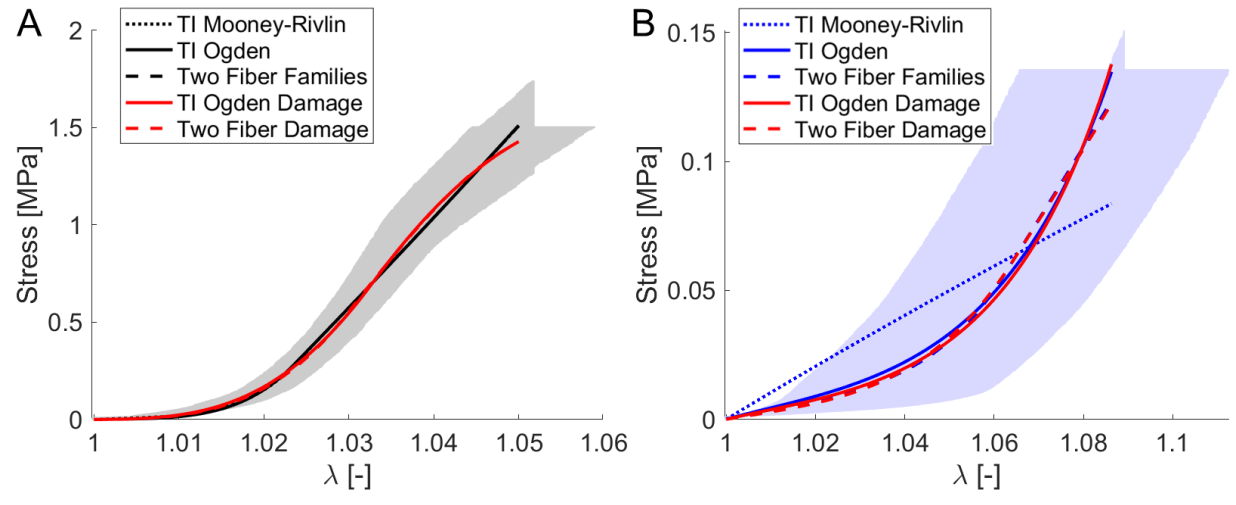


Figure 6. Comparison between biaxial experimental data and model in A) longitudinal direction and B) transverse direction. Note the significant model overlap.

Table 2. Statistical evaluations of model fits to experimental data.

Model	Percent Error	Goodness of Fit	RMSE [MPa]
TI Mooney-Rivlin	87.9	0.945	0.0233
TI Ogden	33.7	0.952	0.0204
Two Fiber Families	25.2	0.953	0.0198
TI Ogden Damage	24.3	0.984	0.00665
Two Fiber Damage	19.0	0.984	0.00655

Model parameters for all five formulations (Table 3) show a longitudinal fiber modulus value of approximately 50 MPa and a transverse modulus of approximately 2.4 MPa. The λ^* values also suggest that the longitudinal fibers are fully recruited at stretch values between 1.02 and 1.03, while the transverse response exhibited a larger toe-region with full fiber recruitment occurring at approximately 1.06-1.065 (Table 3). The transversely isotropic Ogden model exhibited both strong fitting statistics and a low number of fitting parameters (five), while the two fiber families with damage formulation exhibited the best fitting statistics and enables the use of damage modeling, but requires nearly twice the parameters (nine).

Table 3. Biaxial finite element model parameter values.

Model	c ₁ [MPa]	<i>m</i> ₁ [-]	E_f [MPa]	β [-]	λ* [-]	σ [-]	μ [-]
TI Mooney-Rivlin	0.0493	-	43.3	5.17	1.0233	-	-
TI Ogden	0.185	41.0	44.0	4.82	1.0234	-	-
Two Fiber Families	0.0172		44.3	4.76	1.0237	-	-
I wo riber rainines	0.0172	-	2.35	5.21	1.0619	-	-
TI Ogden Damage	0.157	44.2	69.8	4.02	1.0327	0.509	0.118
Two Fiber Damage	0.0135		55.1	4.06	1.0296	0.316	0.122
Two Floer Damage		-	2.37	4.34	1.0643	-	-

3.3 Scanning Electron Microscopy

Scanning electron microscopy (SEM) of aponeurosis at different magnifications shows a composite hierarchical structure with highly aligned collagenous sheets and collagen cables (Figure 7). Superficial collagen cables (Figure 7A) appear to have some degree of random organization, while a collagen fibril sheet (Figure 7B) is comprised of highly aligned collagen fibrils. In addition to variation in structure, collagen fibril sheets appear to have a variation in waviness (Figure 7C). Characterization of fiber dispersion shows that the directional alignment in aponeurosis can very from highly aligned and straight fibers (dispersion standard deviation of ~7 degrees, Table 4) to a more dispersed case (~30 degrees, Table 4).

Table 4. Gaussian distribution fit dispersion (standard deviation of Gaussian fit) and goodness of fit for analyzed scanning electron microscopy images.

Image	Dispersion [deg]	Goodness of Fit [-]
Straight Image	6.94	0.97

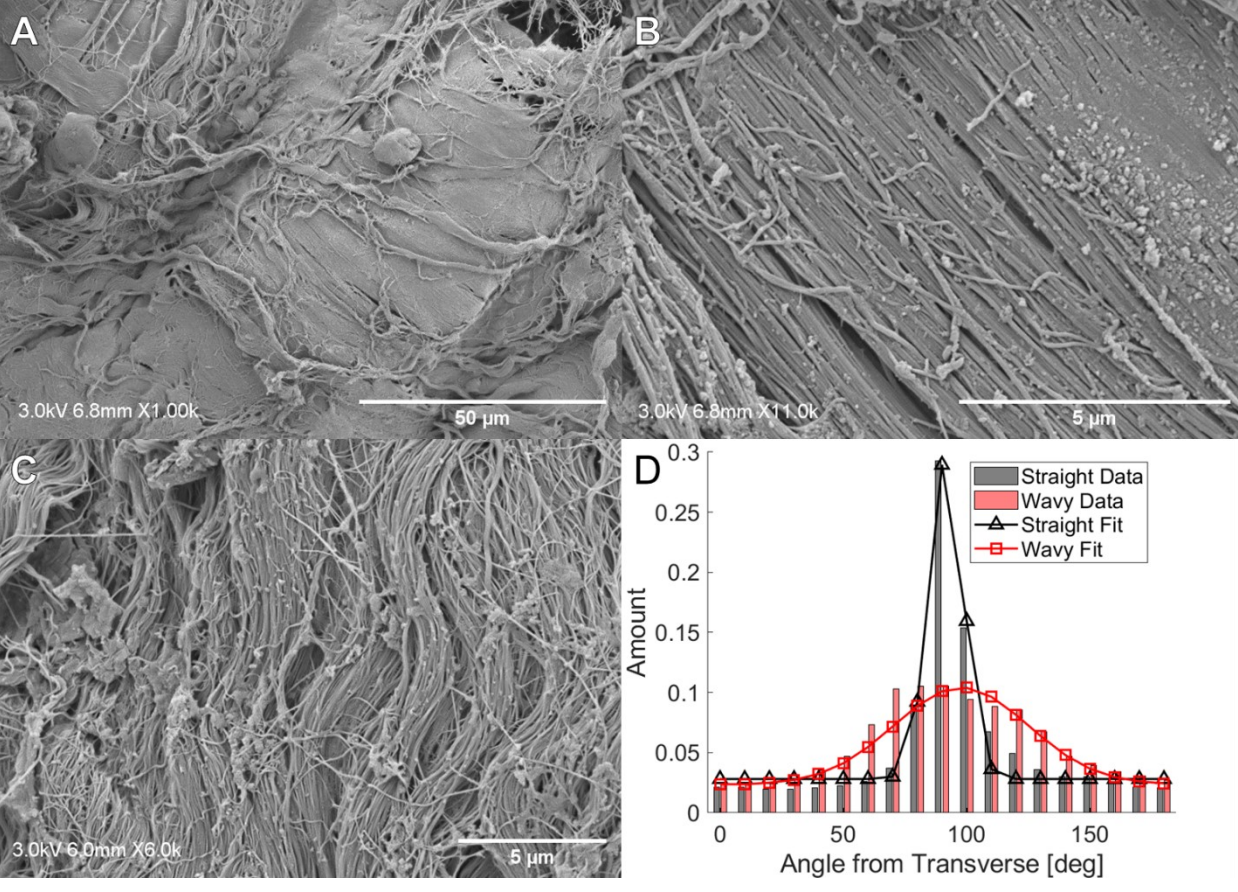


Figure 7. Scanning electron microscopy of aponeurosis tissue and analysis of fiber alignment. A) Image showing aligned collagen sheet under collagen cables. B) Higher magnification of aligned fiber sheet with straight fibrils ("Straight") taken from a region in A. C) Higher magnification of aligned fiber sheet with wavy fibrils ("Wavy") taken from a region not shown in A. D) Comparison of collagen fibril alignment image analysis data and normal distribution fits for the images in B and C. Note that data are plotted as a function of angle from the transverse direction, or that a value of 90° indicates the longitudinal direction.

4. Discussion

While the broader goal of the study was to elucidate the mechanical properties of aponeurosis tissue, the four specific goals were: 1) measure the stress-relaxation behavior of aponeurosis tissue and determine if there was strain level dependence (nonlinear viscoelastic or quasi-linear viscoelastic), 2) perform planar biaxial tensile testing to evaluate aponeurosis tissue response to multi-axial load, 3) employ computational modeling based on the above to develop the appropriate material properties of aponeurosis, and 4) perform scanning electron microscopy to visually determine collagen organization in aponeurosis.

4.1 Stress Relaxation

When considering both statistical analysis (Figure 3) and viscoelastic fitting (Table 1 and Figure 4), we conclude that from approximately 1-4% tensile strain, aponeurosis relaxation behavior is comparable.

While a statistically significant result between power law parameters for the two relaxation steps was found (p=0.044), this represents a case where the data may be statistically different but not functionally different. These results support the claim that the aponeurosis exhibits quasi-linear viscoelastic behavior (Pavan et al., 2014), similar to other fibrous connective tissues like tendon (Taylor et al., 1990; Johnson et al., 1994; Provenzano et al., 2001). Qualitative examination of digital image correlation strain plots suggests that the aponeurosis does not strain in a homogenous manner due to the non-uniform recruitment of collagen fibers and fascicles during uniaxial tensile testing. These findings are similar to a previous study that showed that the aponeurosis-tendon unit strained nonuniformly when submaximal voluntary contractions occurred in vivo (Finni et al., 2003). While characterization of this inhomogeneous strain was outside of the scope of this work, future efforts to measure regional aponeurosis strain would be a benefit to the field. One limitation of the material tests performed in this work is the lack of tissue immersion in a buffering solution. This was chosen for comparative purposes to other studies of aponeurosis material properties that tested in non-immersed conditions (Azizi et al., 2009; Shan et al., 2019), to improve digital image correlation analysis, and to introduce as few variables into the testing protocol as various buffer solutions can affect measured mechanical properties (Safa et al., 2017). However, future work to evaluate the effect of various buffer solutions, graphite powder speckling and dehydration, and of immersed versus non-immersed conditions could further improve the translation of in vitro data to in vivo models and considerations.

Viscoelastic fitting of the three-term linear Prony series model to the normalized experimental data show an excellent ability of this approach to fit stress-relaxation data. As highlighted above, the similar viscoelastic model parameters optimized for both stress-relaxation ramps and the accuracy of a fit to mean data suggest the parameters provided in Table 1 could be reasonably used for future modeling efforts. One limitation of this work is that only normalized stress relaxation data was used in the viscoelastic model, which was completed for simplicity. Additionally, these viscoelastic parameters were not validated against independent data, and as such they should only be used for simulations of similar or slower strain-rate conditions. Future studies could incorporate and couple the stress-relaxation and stress-stretch data presented in this study to other viscoelastic models and perform validation experiments.

4.2 Biaxial Stretch

To the best of the authors' knowledge, there exists only two previous studies that have directly measured stress-stretch material properties of aponeurosis (Azizi et al., 2009; Shan et al., 2019). Azizi et al., 2009 measured the anisotropic linear modulus and failure properties of turkey gastrocnemius aponeurosis and found that the longitudinal direction had a higher tensile modulus (~700 MPa) value compared to the transverse direction (~100 MPa). Shan et al. studied the morphological and mechanical characteristics of the human triceps surae aponeuroses in various regions of the gastrocnemius and soleus, determining that thickness varied depending on location and a similarly higher modulus in the longitudinal (64-145 MPa) versus transverse (0.3-1.5 MPa) directions (Shan et al., 2019). Our linear region modulus results presented here were generated by constitutive model fitting via inverse finite element analysis. The findings of a longitudinal modulus of ~50 MPa and transverse modulus of ~2 MPa agree well with Shan et al. In comparing these values to tensile moduli for tendon and muscle, we see that aponeurosis tissue

compares similarly to tendon and is approximately 1-2 orders of magnitude stiffer than muscle (Table 5). This suggests that aponeurosis functions from a materials perspective as an extension of tendon and not as a transition from tendon to muscle. However, this requires further extensive material testing of aponeurosis and tendon from the same muscle-tendon unit to confirm. Despite the range of reported moduli values for aponeurosis in literature (Table 5), our findings corroborate the observation that the aponeurosis is stiffer in the longitudinal direction compared to the transverse direction and that the transverse direction experienced more stretch during the experiment (Figure 5) (Azizi and Roberts, 2009; Azizi et al., 2009).

Table 5. Comparison between anisotropic linear-region tensile elastic modulus values reported in literature and those presented in this study for tendon, aponeurosis, and muscle tissue. Note that * denotes some approximate values for skeletal muscle stress-stretch curve tangents, as muscle exhibits a great degree of nonlinearity.

Tissue	Longitudinal Modulus [MPa]	Transverse Modulus [MPa]	References
Tendon	50-1850	0.2-40	(Wren et al., 2001; Lynch et al., 2003; Lake et al., 2009, 2010)
Aponeurosis	50-750	0.3-100	Our work and (Azizi et al., 2009; Shan et al., 2019)
Muscle*	0.02-0.5	0.08-0.4	(Takaza et al., 2012; Mohammadkhah et al., 2016; Wheatley et al., 2016b)

One cautious observation of this work is the relatively large size of the error bars on the transverse stress-stretch graph (Figure 6B). We believe this is due to specimen variability, anisotropic strain in aponeurosis, and the highly anisotropic nature of the tissue. As the transverse direction is not the major load bearing direction of the tissue, a larger variability of strain values was expected. Future work could experiment with different strain ratios and strain rates in the longitudinal and transverse directions to determine how the aponeurosis responds mechanically to non-equibiaxial stretch. This could also potentially reduce the variability of stretch observed in the transverse direction.

As discussed above, there exists limited published data on the material properties of aponeurosis tissue. To the best of the authors' knowledge, there exists no prior study that has fit anisotropic, hyperelastic constitutive models to aponeurosis stress-stretch data. Thus, we have presented here not only the first such complete model parameters, but also various modeling approaches for future implementation depending on potential application. We chose five anisotropic constitutive models to employ in this work, ranging from more common isotropic matrix models with a single set of reinforcing fibers (TI Mooney-Rivlin) to a model with multiple fiber families and longitudinal fiber damage (Two Fiber Damage). These five models are not fully comprehensive of all modeling procedures, but nonetheless provide different advantages and disadvantages.

In comparing model fits to experimental stress-stretch data, all of the models exhibited a strong fit to longitudinal data (Figure 6A), and all models except the TI Mooney-Rivlin case exhibited similarly strong fits to transverse data (Figure 6B). As the TI Ogden model requires fewer parameters in comparison to the Two Fiber Families model (five versus seven), we recommend use of this formulation for general modeling procedures. In the case where a user may want to include damage (such as a simulation of extreme stretch or potential rupture), we recommend the use of the TI Ogden Damage approach. While it may seem redundant to implement the Two Fiber Family model, this approach provided outputs of longitudinal and transverse fiber modulus values as discussed above in detail.

The damage modeling employed in this work provides a general application of damage modeling of aponeurosis at quasi-static strain rates and under controlled strain. As damage accumulation in this work was defined as a function of normal Lagrange strain, tissue damage does not directly depend on any stress measures. These stress measures could be backed out from the normal Lagrange strain measures under which damage reaches 50% (Table 3). We believe that using strain as a damage initiation measure is more appropriate than stress because variations in aponeurosis linear modulus in literature are approximately an order of magnitude, while damage initiation in soft tissues is surely bounded by a much smaller stretch region. For example, it is unlikely that the turkey gastrocnemius aponeurosis tested by Azizi et al (Azizi et al., 2009) would accumulate damage when subject to similar stress states to the porcine triceps brachii tested in this work due the measured linear modulus value of nearly ~700 MPa compared to ~50 MPa measured here. However, qualitative comparisons of pull to failure stress-stretch curves from Azizi et al show longitudinal failure at approximately $\lambda \approx 1.075$, with damage likely initiating in the $\lambda \approx 1.03$ – 1.05 range, which is similar to our modeling results. Future modeling efforts to better characterize the damage accumulation and failure, particularly at high strain rates would elucidate how aponeurosis rupture occurs and how it could be modeled. Multi-axial damage modeling would also be a benefit, although it is more likely that in vivo aponeurosis damage and muscle-tendon unit impairment is related to longitudinal loading.

For biological soft tissues, the assumption of incompressibility or near-incompressibility (Weiss et al., 1996) is common due to their high water content, thus requiring the use of decoupled strain energy formulations to prevent volume-locking of elements. However, to the best of the author's knowledge, there exists no experimental investigations of the volumetric behavior of aponeurosis. Due to the sheet-like macroscopic structure of aponeurosis, it is unlikely that maintaining constant volume plays a critical role in the tissue function relative to the tensile stiffness of the material. Thus, to increase model stability and reduce assumptions and complexity, we selected a bulk modulus of 100 MPa and employed a coupled hyperelastic formulation without experiencing volume locking. Further experimental analysis to directly evaluate the volumetric behavior of aponeurosis would provide necessary data to adjust the modeling assumptions made in this work.

4.4 Scanning Electron Microscopy

We employed scanning electron microscopy (SEM) to provide a qualitative comparison of aponeurosis microstructure to the mechanical testing and modeling. Previous efforts have used high magnification

oblique contrast microscopy, which limits visualization to collagen fascicles (Azizi et al., 2009). To the authors' knowledge, no previous studies have conducted scanning electron microscopy on the aponeurosis; however, it has been shown that type I collagen is the dominant fiber type (Miao et al., 2019). Our SEM images suggest that the aponeurosis is comprised of both collagenous cables and sheets (Figure 7A) and that these sheets contain collagen fibrils with some variability of waviness and/or dispersion (7B-D). We expect that as the aponeurosis is stretched, the regions with waviness (also referred to as crimping) become straight, and that this is the mechanism for the toe-region in the stress-stretch experimental data and modeling results presented here. Thus, there is a general agreement (although not numerically quantified) between our microstructural analysis and the macroscale experimentation and modeling.

While we have not generated microstructurally driven computational models of the aponeurosis, further rigorous SEM could generate the data necessary to inform such models. The specific hyperelastic formulation chosen here to represent collagenous structures in the aponeurosis (Equation 11) includes a nonlinear toe-region during which collagenous structures uncrimp. However, the λ^* values were optimized from stress-stretch data and not generated from SEM images. Additional implementations of dispersed fiber models (von Hoegen et al., 2019) driven by microstructure (Figure 7D) could greatly strengthen modeling efforts of aponeurosis and muscle-tendon units.

5. Conclusion

This work presents an investigation of the mechanical properties of aponeurosis tissue through stress relaxation testing, planar biaxial testing, constitutive modeling and finite element analysis, and characterization of microstructure through scanning electron microscopy. In all, the study found that the aponeurosis exhibits nearly linear stress-relaxation behavior, highly anisotropic hyperelastic behavior, and has intricate microstructural collagen fibril alignment. We have presented viscoelastic parameters for future modeling use as well as and anisotropic, hyperelastic, and damage constitutive parameters for similar use. Future use to drive modeling efforts with microstructural data would be a natural continuation of this work and would be a benefit to the field. Generally, this work helps to better understand aponeurosis material properties and thus how aponeurosis transmits force and stores (and returns) energy during movement.

6. Acknowledgements and Conflicts of Interest

- Funding for equipment used in this work was provided by the National Science Foundation under Major Research Instrumentation Grant No. 1828082.
- The authors would also like to acknowledge the Program for Undergraduate Research (PUR) at Bucknell University for financial support.
- No disclosures or conflicts of interest to report.

7. References

607

608

609

610

611

612

613

614 615

616

617

618

619

620

623 624

625

626 627

628

629

630

631

- Ackland, D. C., Lin, Y. C., and Pandy, M. G. (2012). Sensitivity of model predictions of muscle function to changes in moment arms and muscle-tendon properties: A Monte-Carlo analysis. *J. Biomech.* 45, 1463–1471. doi:10.1016/j.jbiomech.2012.02.023.
- Arellano, C. J., Gidmark, N. J., Konow, N., Azizi, E., and Roberts, T. J. (2016). Determinants of
 aponeurosis shape change during muscle contraction. *J. Biomech.* doi:10.1016/j.jbiomech.2016.04.022.
 - Azizi, E., Halenda, G. M., and Roberts, T. J. (2009). Mechanical properties of the gastrocnemius aponeurosis in wild turkeys. *Integr. Comp. Biol.* 49, 51–8. doi:10.1093/icb/icp006.
 - Azizi, E., and Roberts, T. J. (2009). Biaxial strain and variable stiffness in aponeuroses. *J. Physiol.* 587, 4309–18. doi:10.1113/jphysiol.2009.173690.
 - Bojsen-Møller, J., and Magnusson, S. P. (2019). Mechanical properties, physiological behavior, and function of aponeurosis and tendon. *Rev. Passiv. Prop. Muscle J Appl Physiol* 126, 1800–1807. doi:10.1152/japplphysiol.00671.2018.-During.
 - Carson, F. L., and Cappellano, C. H. (1997). *Histotechnology: A Self-Instructional Text 4th Edition*. 2nd ed. American Society of Clinical Pathologists Press.
 - Chen, T. (2000). Determining Viscoelastic Strain Data a Prony Material Series for a From Time Varying. 26.
 - Eng, C. M., Pancheri, F. Q., Lieberman, D. E., Biewener, A. A., and Dorfmann, L. (2014). Directional differences in the biaxial material properties of fascia lata and the implications for fascia function. *Ann. Biomed. Eng.* 42, 1224–1237. doi:10.1007/s10439-014-0999-3.
- Eng, C. M., and Roberts, T. J. (2018). Aponeurosis influences the relationship between muscle gearing
 and force. 125, 513–519. Available at:
 - https://www.physiology.org/doi/10.1152/japplphysiol.00151.2018 [Accessed November 21, 2019].
 - Evans, J. H., and Barbenel, J. C. (1975). Structural and Mechanical Properties of Tendon related to Function. *Equine Vet. J.* 7, 1–8. doi:10.1111/j.2042-3306.1975.tb03221.x.
 - Finni, T., Hodgson, J. A., Lai, A. M., Edgerton, V. R., and Sinha, S. (2003). Nonuniform strain of human soleus aponeurosis-tendon complex during submaximal voluntary contractions in vivo. *J. Appl. Physiol.* 95, 829–837. doi:10.1152/japplphysiol.00775.2002.
 - Herod, T. W., Chambers, N. C., and Veres, S. P. (2016). Collagen fibrils in functionally distinct tendons have differing structural responses to tendon rupture and fatigue loading. *Acta Biomater*. 42, 296–307. doi:10.1016/j.actbio.2016.06.017.
 - Herzog, W. (2017). Skeletal muscle mechanics: Questions, problems and possible solutions Daniel P Ferris. *J. Neuroeng. Rehabil.* 14. doi:10.1186/s12984-017-0310-6.
- Herzog, W. (2019). The problem with skeletal muscle series elasticity. *BMC Biomed. Eng.* 1, 28.
 doi:10.1186/s42490-019-0031-y.
- Jacobs, N. T., Cortes, D. H., Vresilovic, E. J., and Elliott, D. M. (2013). Biaxial tension of fibrous tissue:
 Using finite element methods to address experimental challenges arising from boundary conditions and anisotropy. *J. Biomech. Eng.* 135, 1–10. doi:10.1115/1.4023503.
- Johnson, G. A., Tramaglini, D. M., Levine, R. E., Ohno, K., Choi, N. -Y, and L-Y. Woo, S. (1994).
 Tensile and viscoelastic properties of human patellar tendon. *J. Orthop. Res.* 12, 796–803.
 doi:10.1002/jor.1100120607.
- Kitaoka, H. B., Ping Luo, Z., Growney, E. S., Lawrence Berglund, S. J., and An, K.-N. (1994). Material
 Properties of the Plantar Aponeurosis.
- Komatsu, K., Sanctuary, C., Shibata, T., Shimada, A., and Botsis, J. (2007). Stress-relaxation and
 microscopic dynamics of rabbit periodontal ligament. *J. Biomech.* 40, 634–644.
 doi:10.1016/j.jbiomech.2006.01.026.
- Labus, K. M., and Puttlitz, C. M. (2016). An anisotropic hyperelastic constitutive model of brain white matter in biaxial tension and structural–mechanical relationships. *J. Mech. Behav. Biomed. Mater.* 62, 195–208. doi:10.1016/j.jmbbm.2016.05.003.

- Lake, S. P., Miller, K. S., Elliott, D. M., and Soslowsky, L. J. (2009). Effect of fiber distribution and realignment on the nonlinear and inhomogeneous mechanical properties of human supraspinatus tendon under longitudinal tensile loading. *J. Orthop. Res.* 27, 1596–1602. doi:10.1002/jor.20938.
- Lake, S. P., Miller, K. S., Elliott, D. M., and Soslowsky, L. J. (2010). Tensile properties and fiber alignment of human supraspinatus tendon in the transverse direction demonstrate inhomogeneity, nonlinearity, and regional isotropy. *J. Biomech.* 43, 727–732. doi:10.1016/j.jbiomech.2009.10.017.
 - Luyckx, T., Verstraete, M., De Roo, K., De Waele, W., Bellemans, J., and Victor, J. (2014). Digital image correlation as a tool for three-dimensional strain analysis in human tendon tissue. *J. Exp. Orthop.* 1, 1–9. doi:10.1186/s40634-014-0007-8.
 - Lynch, H. A., Johannessen, W., Wu, J. P., Jawa, A., and Elliott, D. M. (2003). Effect of Fiber Orientation and Strain Rate on the Nonlinear Uniaxial Tensile Material Properties of Tendon. *J. Biomech. Eng.* 125, 726–731. doi:10.1115/1.1614819.
 - Maas, S. A., Ellis, B. J., Ateshian, G. A., and Weiss, J. A. (2012). FEBio: finite elements for biomechanics. *J. Biomech. Eng.* 134, 011005. doi:10.1115/1.4005694.

657

658

659

660

661

662

663

664

665

666

667

668

669

670

671

672

679

680

681

685

686

693

694

- Miao, X., Shan, T., and Wang, J. (2019). The Type and Content of Collagen Fibers of The Levator Aponeurosis In Simple Congenital Blepharoptosis Patients. *J. Craniofac. Surg.* doi:10.1097/scs.000000000006135.
- Mohammadkhah, M., Murphy, P., and Simms, C. K. (2016). The in vitro passive elastic response of chicken pectoralis muscle to applied tensile and compressive deformation. *J. Mech. Behav. Biomed. Mater.* 62, 468–480. doi:10.1016/j.jmbbm.2016.05.021.
- Mohammadkhah, M., Simms, C. K., and Murphy, P. (2017). Visualisation of Collagen in fixed skeletal muscle tissue using fluorescently tagged Collagen binding protein CNA35. doi:10.1016/j.jmbbm.2016.10.022.
- Ong, C. F., Geijtenbeek, T., Hicks, J. L., and Delp, S. L. (2019). Predicting gait adaptations due to ankle
 plantarflexor muscle weakness and contracture using physics-based musculoskeletal simulations.
 PLoS Comput. Biol. 15, e1006993. doi:10.1371/journal.pcbi.1006993.
- Pavan, P. G., Pachera, P., Stecco, C., and Natali, A. N. (2014). Constitutive modeling of time-dependent response of human plantar aponeurosis. *Comput. Math. Methods Med.* 2014.
 doi:10.1155/2014/530242.
 - Pavan, P. G., Stecco, C., Darwish, S., Natali, A. N., and De Caro, R. (2011). Investigation of the mechanical properties of the plantar aponeurosis. *Surg. Radiol. Anat.* 33, 905–911. doi:10.1007/s00276-011-0873-z.
- Pioletti, D. P., and Rakotomanana, L. R. (2000). On the independence of time and strain effects in the stress relaxation of ligaments and tendons. *J. Biomech.* 33, 1729–1732. doi:10.1016/S0021-9290(00)00128-7.
 - Provenzano, P., Lakes, R., Keenan, T., and Vanderby, R. (2001). Nonlinear ligament viscoelasticity. *Ann. Biomed. Eng.* 29, 908–914. doi:10.1114/1.1408926.
- Provenzano, P. P., and Vanderby, R. (2006). Collagen fibril morphology and organization: Implications for force transmission in ligament and tendon. *Matrix Biol.* 25, 71–84.
 doi:10.1016/j.matbio.2005.09.005.
- Rajagopal, A., Dembia, C. L., DeMers, M. S., Delp, D. D., Hicks, J. L., and Delp, S. L. (2016). Full-Body
 Musculoskeletal Model for Muscle-Driven Simulation of Human Gait. *IEEE Trans. Biomed. Eng.* 63, 2068–79. doi:10.1109/TBME.2016.2586891.
 - Rehorn, M. R., and Blemker, S. S. (2010). The effects of aponeurosis geometry on strain injury susceptibility explored with a 3D muscle model. *J. Biomech.* 43, 2574–81. doi:10.1016/j.jbiomech.2010.05.011.
- Safa, B. N., Meadows, K. D., Szczesny, S. E., and Elliott, D. M. (2017). Exposure to buffer solution alters tendon hydration and mechanics. *J. Biomech.* 61, 18–25. doi:10.1016/j.jbiomech.2017.06.045.
- Safa, B. N., Santare, M. H., and Elliott, D. M. (2018). A Reactive Inelasticity Theoretical Framework for
 Modeling Viscoelasticity, Plastic Deformation, and Damage in Fibrous Soft Tissue. *J. Biomech.* Eng. 141, 021005. doi:10.1115/1.4041575.

- Schindelin, J., Arganda-Carreras, I., Frise, E., Kaynig, V., Longair, M., Pietzsch, T., et al. (2012). Fiji: An open-source platform for biological-image analysis. *Nat. Methods* 9, 676–682.
 doi:10.1038/nmeth.2019.
- Scott, S. H., and Loeb, G. E. (1995). Mechanical Properties of Aponeurosis and Tendon of the Cat Soleus
 Muscle During Whole-Muscle Isometric Contractions.

- Shan, X., Otsuka, S., Yakura, T., Naito, M., Nakano, T., and Kawakami, Y. (2019). Morphological and mechanical properties of the human triceps surae aponeuroses taken from elderly cadavers: Implications for muscle-tendon interactions. *PLoS One* 14. doi:10.1371/journal.pone.0211485.
- Sleboda, D. A., Stover, K. K., and Roberts, T. J. (2020). Diversity of extracellular matrix morphology in vertebrate skeletal muscle. *J. Morphol.* 281, 160–169. doi:10.1002/jmor.21088.
- Szczesny, S. E., Peloquin, J. M., Cortes, D. H., Kadlowec, J. A., Soslowsky, L. J., and Elliott, D. M. (2012). Biaxial Tensile Testing and Constitutive Modeling of Human Supraspinatus Tendon. *J. Biomech. Eng.* 134, 021004. doi:10.1115/1.4005852.
- Takaza, M., Moerman, K. M., Gindre, J., Lyons, G., and Simms, C. K. (2012). The anisotropic mechanical behaviour of passive skeletal muscle tissue subjected to large tensile strain. *J. Mech. Behav. Biomed. Mater.* 17, 209–220. doi:10.1016/j.jmbbm.2012.09.001.
- Taylor, D. C., Dalton, J. D., Seaber, A. V., and Garrett, W. E. (1990). Viscoelastic properties of muscle-tendon units: The biomechanical effects of stretching. *Am. J. Sports Med.* 18, 300–309. doi:10.1177/036354659001800314.
- Tsui, C. P., Tang, C. Y., Leung, C. P., Cheng, K. W., Ng, Y. F., Chow, D. H. K., et al. (2004). Active finite element analysis of skeletal muscle-tendon complex during isometric, shortening and lengthening contraction. *Biomed. Mater. Eng.*
- Vaidya, A. J., and Wheatley, B. B. (2019). An experimental and computational investigation of the effects of volumetric boundary conditions on the compressive mechanics of passive skeletal muscle. *J. Mech. Behav. Biomed. Mater.*, 103526. doi:10.1016/j.jmbbm.2019.103526.
- von Hoegen, M., Marino, M., Schröder, J., and Wriggers, P. (2019). Direct and inverse identification of constitutive parameters from the structure of soft tissues. Part 2: dispersed arrangement of collagen fibers. *Biomech. Model. Mechanobiol.*, 1–24. doi:10.1007/s10237-019-01119-3.
- Wager, J. C., and Challis, J. H. (2016). Elastic energy within the human plantar aponeurosis contributes to arch shortening during the push-off phase of running. *J. Biomech.* 49, 704–709. doi:10.1016/j.jbiomech.2016.02.023.
- Weiss, J. A., Maker, B. N., and Govindjee, S. (1996). Finite element implementation of incompressible, transversely isotropic hyperelasticity. *Comput. Methods Appl. Mech. Eng.* 135, 107–128. doi:10.1016/0045-7825(96)01035-3.
- Wheatley, B. B. B., Morrow, D. A., Odegard, G. M. G. M., Kaufman, K. R. K. R., and Haut Donahue, T. L. T. L. (2016a). Skeletal muscle tensile strain dependence: Hyperviscoelastic nonlinearity. *J. Mech. Behav. Biomed. Mater.* 53, 445–454. doi:10.1016/j.jmbbm.2015.08.041.
- Wheatley, B. B., Fischenich, K. M., Button, K. D., Haut, R. C., and Haut Donahue, T. L. (2015). An optimized transversely isotropic, hyper-poro-viscoelastic finite element model of the meniscus to evaluate mechanical degradation following traumatic loading. *J. Biomech.* 48. doi:10.1016/j.jbiomech.2015.02.028.
- Wheatley, B. B., Odegard, G. M., Kaufman, K. R., and Donahue, T. L. H. (2016b). How does tissue preparation affect skeletal muscle transverse isotropy? *J. Biomech.* 49, 3056–3060. doi:10.1016/j.jbiomech.2016.06.034.
- Wheatley, B. B., Odegard, G. M., Kaufman, K. R., and Haut Donahue, T. L. (2018). Modeling Skeletal
 Muscle Stress and Intramuscular Pressure: A Whole Muscle Active-Passive Approach. *J. Biomech.* Eng. 140, 081006. doi:10.1115/1.4040318.
- Wheatley, B. B., Pietsch, R. B., Haut Donahue, T. L., and Williams, L. N. (2016c). Fully non-linear
 hyper-viscoelastic modeling of skeletal muscle in compression. *Comput. Methods Biomech. Biomed. Engin.* 19. doi:10.1080/10255842.2015.1118468.
- Wren, T. A. L., Yerby, S. A., Beaupré, G. S., and Carter, D. R. (2001). Mechanical properties of the